

Resonance frequency above 20 GHz in superparamagnetic NiZn-ferrite

Cite as: Appl. Phys. Lett. **121**, 062402 (2022); <https://doi.org/10.1063/5.0102965>

Submitted: 14 June 2022 • Accepted: 21 July 2022 • Published Online: 09 August 2022

 Sarath Arackal, Kouhei Nozawa,  Ralandinliu Kahmei, et al.



View Online



Export Citation



CrossMark

ARTICLES YOU MAY BE INTERESTED IN

[Opportunities for nitrogen-vacancy-assisted magnetometry to study magnetism in 2D van der Waals magnets](#)

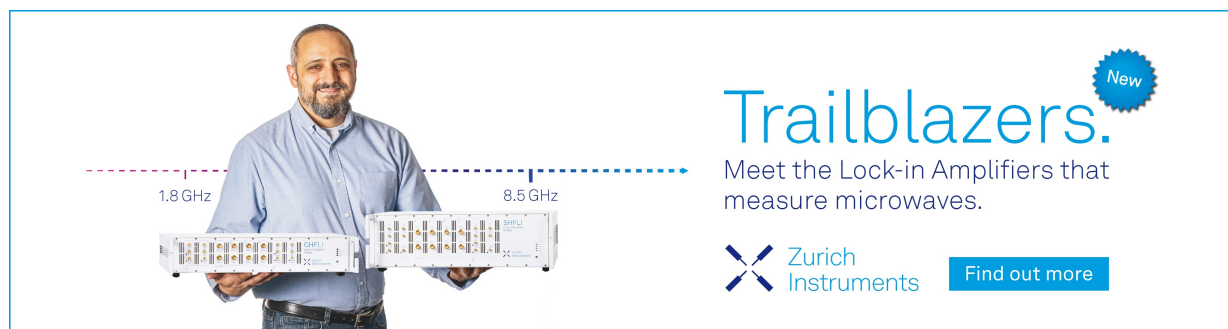
Applied Physics Letters **121**, 060502 (2022); <https://doi.org/10.1063/5.0091931>


[Electrostatic control of magnetism: Emergent opportunities with van der Waals materials](#)

Applied Physics Letters **121**, 060501 (2022); <https://doi.org/10.1063/5.0107329>


[Towards merged-element transmons using silicon fins: The FinMET](#)

Applied Physics Letters **121**, 064001 (2022); <https://doi.org/10.1063/5.0104950>



Trailblazers. 

Meet the Lock-in Amplifiers that measure microwaves.

 Zurich Instruments [Find out more](#)

Resonance frequency above 20 GHz in superparamagnetic NiZn-ferrite

Cite as: Appl. Phys. Lett. **121**, 062402 (2022); doi: [10.1063/5.0102965](https://doi.org/10.1063/5.0102965)

Submitted: 14 June 2022 · Accepted: 21 July 2022 ·

Published Online: 9 August 2022



View Online



Export Citation



CrossMark

Sarath Arackal,¹ Kouhei Nozawa,² Ralandinliu Kahmei,¹ Ton That Loi,² Shin Yabukami,² S. A. Shivashankar,¹ Masahiro Yamaguchi,² Navakanta Bhat,¹ and Ranajit Sai^{1,a)}

AFFILIATIONS

¹Centre for Nano Science and Engineering, Indian Institute of Science, Bangalore 560012, India

²Graduate School of Engineering, Tohoku University, 6-6-05 Aoba-Aza-Aramaki, Aoba-ku, Sendai 980-8579, Japan

^{a)} Author to whom correspondence should be addressed: ranajit@ieee.org

ABSTRACT

We investigate the frequency dispersion of complex permeability in the GHz range in superparamagnetic nickel–zinc ferrite thin films with different Ni/Zn ratios using a microstrip probe. The films, comprising crystallites as small as 3 nm and deposited by a microwave-irradiation-assisted solvothermal method, exhibit the coexistence of two resonance characteristics—a ferromagnetic resonance peak (f_r) at ~ 2 GHz and a superparamagnetic resonance peak (f_b) above 20 GHz, breaching Snoek's limit. The high value of f_r is attributed to the high surface anisotropy and far-from-equilibrium distribution of cations in the lattice, while f_b is attributed to the thermally driven superparamagnetic relaxation of ferrite nanocrystallites in the thin films. This work demonstrates the feasibility of employing superparamagnetic ferrite thin films so deposited as excellent CMOS-integrable magnetic components for high-speed and high-frequency electromagnetic device applications.

Published under an exclusive license by AIP Publishing. <https://doi.org/10.1063/5.0102965>

The rapid growth of CMOS technology is driving the demand for compact and fast on-chip components with low power consumption. The development of chip-integrable magnetic materials with high permeability and resonance/cutoff frequency in the microwave and terahertz ranges is becoming indispensable due to its possible application in high-frequency electronics. Even though magnetic metal alloys and oxides like spinel ferrites are both preferred candidates, the latter has the upper hand owing to their high electrical resistance. However, for conventional spinel ferrites, the natural resonance frequency (f_r) falls in the MHz range because of the low magnetocrystalline anisotropy field (H_k).¹ Researchers have successfully introduced additional anisotropy like shape anisotropy,^{2–5} strain-induced anisotropy,^{6–9} and exchange anisotropy^{10–12} to increase f_r . However, the increase is limited by Snoek's law, which states that $\mu f_r \propto M_s$, where μ is the magnetic permeability, f_r is the natural resonance frequency, and M_s is the saturation magnetization. In other words, a simultaneous increase in f_r and permeability is unattainable.

However, nanomaterials in their superparamagnetic state show multiple resonance characteristics.^{13,14} As the particle size decreases, there exists a volume V_p , where the magnetic anisotropy energy (KV_p) of the nanoparticle becomes comparable to the thermal energy ($k_B T$). Under these conditions, the spins can undergo a thermally

driven relaxation/reversal. The frequency of relaxation depends exponentially on the ratio of anisotropy energy and thermal energy and is given by

$$f_b = f_0 \exp\left(\frac{-KV_p}{k_B T}\right). \quad (1)$$

As a result, the permeability dispersion curve in superparamagnets will have two resonances: one for precession around the anisotropy field and the other for relaxation under thermal fluctuation. Several studies have shown that the value of f_b can surpass f_r , breaking Snoek's limit. For example, 9 nm-Fe₃O₄ synthesized via high-temperature (~ 265 °C) organic-phase synthesis with natural resonance at 1.3 GHz showed f_b at 5.3 GHz and was further increased to 6.9 GHz by controlling the intra-particle dipolar interaction.¹³ On the other hand, a f_b of 8.8 nm-Fe₃O₄ is found to be at 1.3 GHz when prepared via a different synthesis method.¹⁴ These examples clearly indicate that the synthesis route and conditions play a dominant role in determining the magnetic resonance characteristic. Even though spinel ferrites or their composites, like Fe₃O₄/silica,^{15,16} Fe₃O₄/MWCNT (multiwalled carbon nanotubes),¹⁷ and cobalt ferrite,¹⁸ show resonance characteristics above Snoek's limit, the f_b is always observed below 10 GHz.

Polycrystalline nickel–zinc ferrite (NZF) thin films prepared by the spin-spray method show excellent high-frequency magnetic characteristics with high permeability (>50) and natural resonance as high as 3 GHz.^{19,20} However, the particle size is in the range of 100–300 nm, and thus, is not superparamagnetic. It will be fascinating to see if Snoek's limit on superparamagnetic NZF thin films can be broken, allowing for applications in high frequency devices, especially in the mm-wave range relevant to 5G technologies.

Nanocrystalline spinel ferrite thin films deposited by low-temperature ($<200^\circ\text{C}$) microwave-irradiation-assisted solvothermal (MAS) deposition comprise densely packed superparamagnetic particles, which exhibit the “far-from-equilibrium” distribution of cations in their crystal structure that is unique to MAS deposition.^{21,22} Owing to the superparamagnetic property and out-of-place cations, the high frequency resonance characteristics of MAS deposited films are expected to exhibit both precession and relaxation mechanisms. In this context, high-frequency magnetic characteristics of the superparamagnetic NZF thin films deposited by the MAS process are investigated here. The evolution of the resonance characteristics under the influence of an external magnetic bias field is also analyzed.

The MAS process is a well-established method used to prepare nanoparticles, organic reagents, and, most recently, thin films.^{23–27} The method uses the microwave dielectric heating of specific solvents and dissolved ions of specific precursor solutes to drive the chemical reaction, resulting in the formation of nanocrystallites of the desired compound. Here, for the deposition of two varieties of NZF thin films, $\text{Ni}_{0.5}\text{Zn}_{0.5}\text{Fe}_2\text{O}_4$ (N50) and $\text{Ni}_{0.75}\text{Zn}_{0.25}\text{Fe}_2\text{O}_4$ (N75), we follow the procedure mentioned elsewhere.²¹ Briefly, the precursors iron (III) acetylacetonate, nickel (II) acetylacetonate, and zinc (II) acetylacetonate are taken in desired stoichiometric quantity and dissolved in a mixture of ethanol and 1-decanol (volume ratio 3:5) to form the reactant solution. The borophosphosilicate glass (BPSG) (300 nm)/Si substrate (1 cm^2) is immersed into this solution and exposed to microwave irradiation (2.4 GHz; 300 W; Discover-SP CEM Corp., USA) for 30 min. After the reaction, the ferrite-coated substrate is removed from the solution, cleaned with ethanol, and dried at 50°C in air. The aforesaid deposition process is repeated to obtain a thicker film.

The secondary electron micrographs from FE-SEM show dense, strongly adherent films with a thickness of 1.9 and $1\ \mu\text{m}$ for N50 and N75 films [Figs. 1(a) and 1(b)], respectively. Grazing angle x-ray diffraction [Fig. 1(c)] using a Cu-K α source reveals a cubic spinel structure in both samples with peaks indexed to the $Fd\bar{3}m$ space group

(ICDD: 00-008-0234, $\text{Ni}_{0.5}\text{Zn}_{0.5}\text{Fe}_2\text{O}_4$) without any impurity phases. The mean crystalline size of the particles (Scherrer's formula) is found to be 3.2 and 2.7 nm for N50 and N75 films, respectively, confirming their nanocrystallinity. The lattice parameters (8.407 Å for N50 and 8.402 Å for N75) extracted from the Nelson-Riley plot (supplementary material Sec. S1) are very close to the bulk value (8.40 Å) of NiZn-ferrite.²⁸ Meanwhile, the presence of another probable spinel, magnetite, is ruled out by XPS analysis (supplementary material Sec. S2). Therefore, the contributions of lattice stress and impurity phases to the effective magnetic anisotropy are deemed to be negligible.

The static magnetic behavior of NZF thin films is characterized using a SQUID magnetometer. As shown in Fig. 2(a), the films N50 and N75 exhibit strong splitting below T_B between the zero-field cooled (ZFC) and field cooled (FC) magnetization curves, where the ZFC curves exhibit a magnetization maximum followed by descent when the temperature decreases to 5 K. Such behavior of the ZFC curves corresponds to a typical superparamagnetic response described by the characteristic blocking temperature T_B , which corresponds to the maximum value of ZFC data. Also, in the FC curve, only a slight drop in magnetization is observed below T_B . This implies that there is a significant interaction between superparamagnetic particles, where in an ideal non-interacting case, FC magnetization increases monotonically below T_B .^{29,30} Figure 2(b) shows the blocking temperature distribution obtained from the derivative $d(M_{FC} - M_{ZFC})/dT$ of experimental data, where the maximum value gives the mean blocking temperature, \bar{T}_B . The difference between the measured T_B and \bar{T}_B reveals that the samples comprise an inhomogeneous size distribution. $T_B = 18\text{ K}$ and $\bar{T}_B = 9\text{ K}$ were obtained for N50, whereas $T_B = 30\text{ K}$ and $\bar{T}_B = 15\text{ K}$ were obtained for N75, i.e., a higher value of T_B and \bar{T}_B for N75 than for N50. Field-dependent FC and ZFC measurements show that the strength of dipolar interaction is larger in N50 than in N75, which may be due to the higher moment of N50 samples (supplementary material Sec. S3). The narrower distribution of \bar{T}_B in N50 [Fig. 2(b)] is the result of the stronger dipolar interaction, which couples several neighboring particles.³¹ The inverse susceptibility (χ^{-1}) derived from the FC measurements with an applied magnetic field of 500 Oe is plotted in Fig. 2(a). Inverse susceptibility vs T of superparamagnets are described as a curve rather than a straight line, as it is with paramagnets. Here, the slope of χ^{-1} increases gradually with temperature as the magnetic order is progressively disrupted by thermal energy, and even at 350 K, for both the films, transition to paramagnetic phase is not complete.

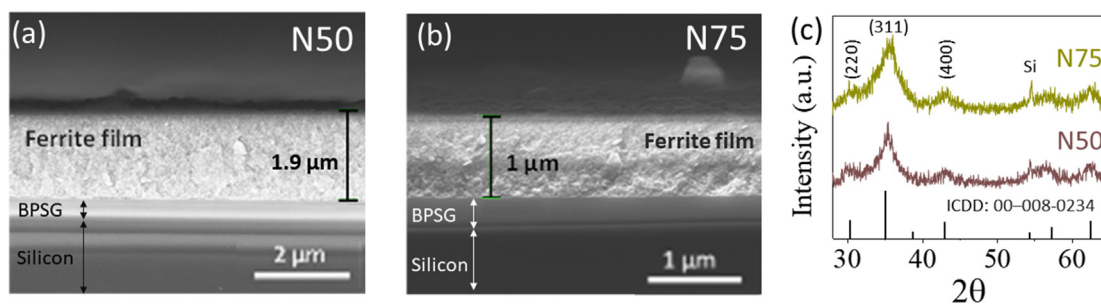


FIG. 1. SEM images show dense, well-adhered nanocrystalline N50 (a) and N75 (b) films on a BPSG/Si substrate. X-ray diffraction shows a spinel structure of N50 and N75 (c).

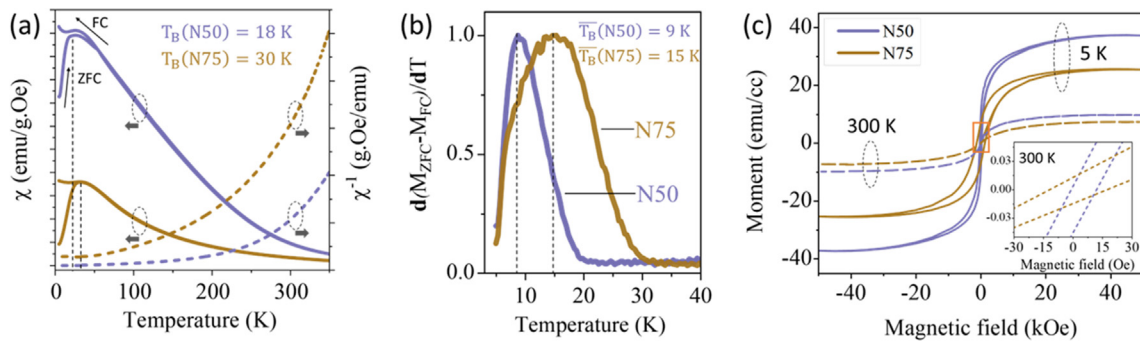


FIG. 2. Magnetic susceptibility derived from the FC/ZFC curves of N50 (solid blue) and N75 (solid yellow) are plotted in (a). Blocking temperature (T_B) is indicated by vertical dashed lines. Inverse susceptibilities (χ^{-1}) of N50 and N75 are represented by blue and yellow broken curves, respectively. (b) Vertical dashed lines indicate the mean blocking temperature (\bar{T}_B) of each sample. Hysteresis curve of N50 and N75 samples at 5 and 300 K is plotted in (c). The inset represents the magnetization values for low fields at 300 K.

Figure 2(c) shows the magnetic hysteresis of N75 and N50 samples measured at 300 and 5 K for an applied field in the range ± 50 kOe. As expected, at 300 K, both samples show superparamagnetic nature with coercivity (H_c) of 6 and 13 Oe [inset, Fig. 2(c)]. The higher value of coercivity in N75 is due to the wider particle size distribution and stronger interparticle magnetic coupling in N75. The saturation magnetization (M_s) measured is higher for N50 than N75 both at 5 and 300 K.

The resonance behavior of the superparamagnetic NiZn ferrite thin films, N50 and N75, is investigated by analyzing the frequency dispersion of complex permeability (μ vs f) in the presence of different external bias fields. The broadband (450 MHz to 55 GHz) permeability of the samples is measured based on a transmission line theory using a “U”-shaped microstrip-line (MSL) probe as reported elsewhere.^{32,33} During the measurements, a 200- μ m thick laminate separates the film from the microstrip line. Calibration is done by saturating the film with a strong bias field ($H_{DC} = 20$ kOe) parallel to the MSL. After calibration, the S-parameters of the MSL in the presence of the film underneath were measured at different bias fields ($H_{DC} = 0, 2, 5, 10,$ and 15 kOe). The impedance change in the electrical circuit due to the magnetic film is manifested as a change in the S-parameters. The complex permeability ($\mu_r = \mu_r' + j\mu_r''$) of the thin film is then determined by using the transmission coefficient (S_{12}) recorded in a VNA (E8361A, Agilent technologies) and an electromagnetic model of the film in an Ansys Maxwell 3D solver.

Figure 3 shows the measured permeability dispersion of N50 and N75, where μ_r' and μ_r'' represent the real and imaginary parts of complex permeability, respectively. The measured permeability of N75 and N50 is ~ 1.5 and ~ 0.5 , respectively. The μ_r'' curve of both samples exhibits two maxima—one at ~ 2 GHz and the other one at ~ 26 GHz, indicating the presence of two resonance phenomena. The nature of the resonance characteristics associated with these peaks, whether they are of ferromagnetic resonance (FMR) f_r and/or superparamagnetic resonance f_b , is confirmed when the shift in these peaks is studied for different H_{DC} , as shown in Figs. 4(a)–4(d). As H_{DC} is increased, one of the peaks shifts toward a higher frequency linearly (supplementary material Sec. S4), while the other one remains unaffected, as depicted in Fig. 4(e). The peak that shifts with bias field is, thus, identified as the ferromagnetic resonance f_r peak, as it follows Kittel's

equation of ferromagnetic resonance in spherical particles, given by $f_r = \gamma(H_k + H_{DC})/2\pi$, where γ is the gyromagnetic ratio and H_k is the magnetocrystalline anisotropy field. Therefore, the ferromagnetic resonance frequency f_r of N75 and N50 is identified at 2.2 and 1.7 GHz, respectively. Both films have a narrow resonance linewidth and a one-to-three-order increase in the FMR frequency in relation to bulk ferrites, which have resonance in the MHz range due to their low anisotropy field^{34–39} but comparable to resonance in nanocrystalline ferrites reported in the literature.^{19,40}

To evaluate the relationship between the effective Gilbert damping constant, α_{eff} , and f_r , we used the equation

$$\alpha_{eff} = \frac{\Delta f}{f_r}, \quad (2)$$

where Δf is the full-width half maximum (FWHM) of the $\mu'' - f$ peak. Δf and f_r values were extracted from fitting the corresponding peak with a Voigt function (supplementary material Sec. S3). As expected, the damping constant decreases with an increase in f_r . The damping constant α_{eff} ranges from 0.45 to 0.04 and 0.3 to 0.06 for N75 and N50, respectively, and is comparable (0.06–0.34) to the values for polycrystalline $\text{Ni}_{0.5}\text{Zn}_{0.5}\text{Fe}_2\text{O}_4$ reported in the literature.²⁰

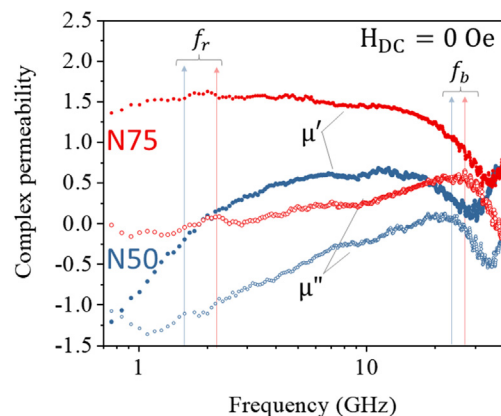


FIG. 3. The plots show frequency dependent complex permeability at zero bias for samples N50 and N75.

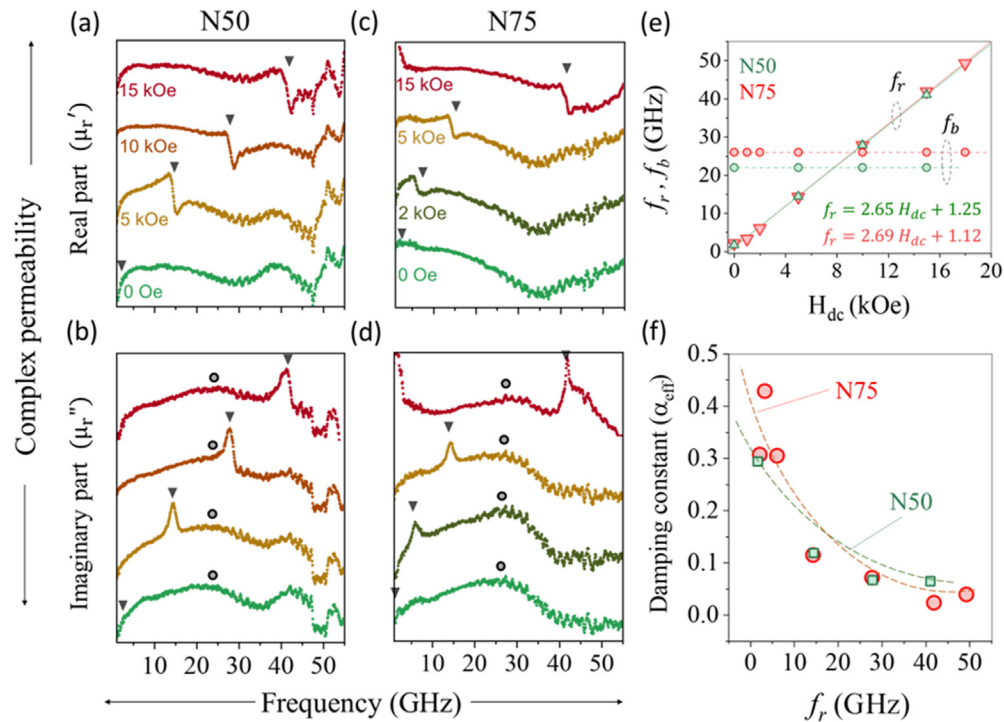


FIG. 4. Effect of magnetic field (H_{DC}) on the resonance characteristics of N50 (a) and (b) and N75 (c) and (d). (a)–(d) With different fields, the change in f_r (triangle) and f_b (circle) is shown. For the sake of clarity, an offset is applied to the y-axis (e). The measured f_r values at different H_{DC} satisfy a linear relationship. (f) Gilbert damping constant (α) derived from $\mu_r'' - f$ plots. The dashed lines are merely a visual aid.

The high FMR frequency of NZF reported here is comparable to other studies reported in the literature¹⁹ and can be attributed to the high magnetic anisotropy of the material. At present, the origin of such high anisotropy is not completely clear. However, two possible reasons are (i) the presence of a far-from-equilibrium cation distribution of magnetic ions, which alters the H_k , and (ii) significant contribution from the surface anisotropy in nanoparticles, owing to the large surface area to volume ratio in fine particles.^{41–43}

Raman spectroscopy has proved to be an effective tool to characterize the distribution of cations in spinel ferrites.^{21,22} Raman spectra were collected by shining a 532 nm laser probe of power 3 mW. The spinel structure displays five Raman active modes, namely, A_{1g} , E_g , and three T_{2g} because of the symmetric and asymmetric bending or stretching of metal–oxygen bonds.⁴⁴ At room temperature, N50 and N75 show three Raman peaks centered at 350, 480, and 680 cm^{-1} (Fig. 5), which correspond to E_g , T_{2g} , and A_{1g} modes, respectively. The peaks at 300 and 520.5 cm^{-1} originate from the substrate. The A_{1g} peak represents the symmetric stretch between metal ions in A-site cations and tetrahedrally coordinated oxygen atoms in the spinel structure. Since different metal–oxygen stretches appear at different wavenumbers, the broad A_{1g} peak at ~ 600 – 750 cm^{-1} in both N50 and N75 suggests the presence of multiple cations in the A-site. The A_{1g} peaks of both samples were deconvoluted by fitting them with individual Lorentzian components. The deconvoluted peaks appearing at 640, 670, and 698 cm^{-1} can be ascribed to the tetrahedrally coordinated Zn–O, Ni–O, and Fe–O stretches, respectively, which, in turn,

indicate the presence of Zn^{2+} , Ni^{2+} , as well as Fe^{3+} at the A-site. By calculating the area under the curve, the concentration of different cations in the A-site is estimated. In line with our previous reports on MAS-synthesized MnZn-ferrite and Zn-ferrite nanoparticles, the thin films presented here also possess a far-from-equilibrium distribution of cations in the crystal.^{21,22} In contrast with bulk crystals and nanoparticles prepared using other synthesis methods,^{45–48} where the A-site occupancy of Ni^{2+} is less than 8%, the ferrites prepared by the MAS process have $>20\%$ of A-sites occupied by Ni^{2+} . Such rearrangement of magnetic ions (Fe^{3+} and Ni^{2+}) in MAS-ferrite nanoparticles can alter the magnetic anisotropy energy landscape and produce a significant increase in the ferromagnetic resonance frequency, as observed in the permeability measurements.

The other important feature of the $\mu_r'' - f$ plot of both N50 and N75 samples is the broad peak at ~ 26 GHz, which remains unaffected by the external bias field. In the literature, the presence of a second resonance peak is usually attributed to superparamagnetic relaxation^{13,14} or antiferromagnetic modes.⁴⁹ In our samples, the possibility of antiferromagnetic resonance (AFR) is unlikely for two reasons: (i) the AFR frequency of ferrites is typically seen in THz regions⁵⁰ and (ii) the microstructural investigations (XRD and Raman spectroscopy) employed were unable to detect any AF oxide phases like nickel oxide (NiO). Hence, the peaks at 26 GHz (N50) and 24 GHz (N75) are likely to be originated from the thermally driven superparamagnetic relaxation (f_b). Also, f_b remains unchanged when H_{DC} is varied, which further confirms

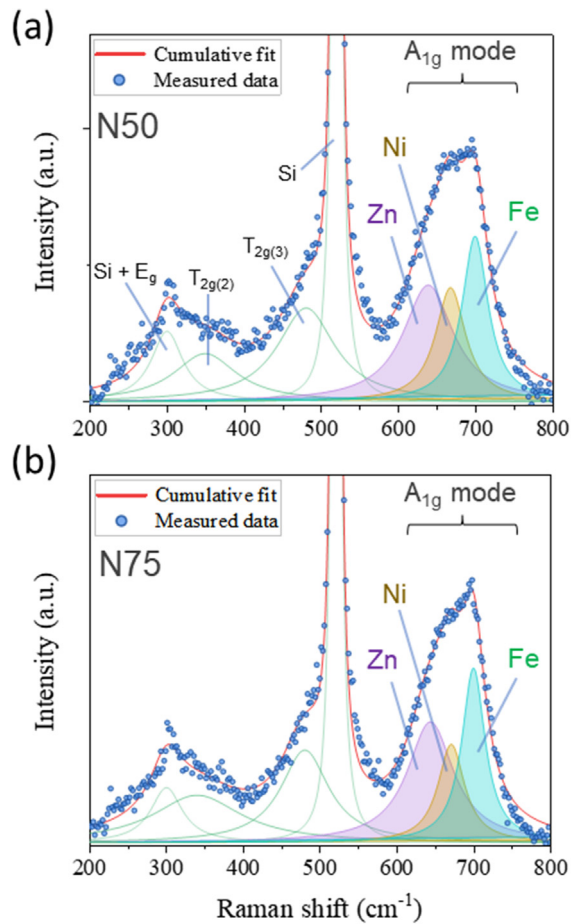


FIG. 5. De-convoluted Raman spectra of (a) N50 and (b) N75. Blue circles: Experimental Raman spectra obtained with a 532 nm laser. Red line: Fit of the data, which represent the sum of individual Lorentzian components.

the assignment of f_b to a thermally driven transition from a superparamagnetic state to a no-response state.

The transition from the superparamagnetic state to a no-response state in iron oxide nanoparticles is studied by Hasegawa *et al.*,¹⁴ wherein the dependence of the relaxation frequency on the ratio between the effective thermal field (H_t) and effective magnetic anisotropy field (H_k) is evaluated. Two cases are considered. In case 1 where $H_t < H_k$, the magnetic nanoparticles undergo transition from the superparamagnetic state to a no response state through a ferromagnetic state, i.e., $f_b < f_r$. On the other hand, in case 2, $H_t > H_k$, where there is a direct transition from the superparamagnetic state to a no-response state, which means $f_b > f_r$. For our samples, the ratio $\frac{H_t}{H_k} = \frac{K_B T}{K V_p} > 1$, i.e., the transition is directly from the superparamagnetic state to a no-response state. Accordingly, the relaxation frequency satisfies the following relation:¹⁴

$$f_b = \frac{\gamma \alpha}{\pi(1 + \alpha^2)} H_t = \frac{\gamma \alpha}{\pi(1 + \alpha^2)} \frac{k_B T}{V_p M_s}, \quad (3)$$

where α is the Gilbert damping parameter under thermal field, V_p is the volume of nanoparticles, and M_s is the saturation magnetization at temperature, T .

Ideally, in Eq. (3), the f_b of N50 should be only two-thirds the value in N75 due to the difference in $V_p M_s$ values. However, in our samples, f_b (N50) is close to f_b (N75). The non-uniform particle size distribution and non-identical local structures lead to differing magnetic interaction, thereby causing discrepancies in measured f_b . Also, the high damping ($\Delta f_b / f_b \sim 1$) nature of the superparamagnetic resonance presented here limits its use in a high-Q, mm-wave device. Understanding the effect of a local structure on magnetic interactions and controlling the same by improving the deposition and/or post-deposition processing are the way forward toward tunable f_b with lower damping values. However, it is beyond the scope of this paper.

In summary, we have demonstrated the coexistence of superparamagnetic and ferromagnetic resonance in thin films comprising well-formed, ultra-fine crystallites of NiZn-ferrite, deposited by a novel microwave-assisted solvothermal (MAS) process. The superparamagnetic resonance frequency ($f_b \approx 26$ GHz), measured using a microstrip-line probe, far exceeds the ferromagnetic resonance frequency ($f_r \approx 2$ GHz), thus pushing the cutoff frequency of NiZn ferrites into the mm-wave range. Ferrite thin films of two different NiZn compositions—N50 and N75—exhibit appreciable permeabilities ($\mu'_r \approx 1.5$) up to 10 GHz with $\tan \delta (= \mu''_r / \mu'_r)$ as low as ≈ 0.17 . The superparamagnetic NiZn ferrite crystallites as small as 3 nm display a very high degree of disorder in the cationic distribution in the lattice, owing to the kinetically driven and “far-from-equilibrium” deposition process employed and resulting in the observed unique high-frequency properties. This finding could spur a plethora of high-frequency device applications, especially in mm-wave magnetics and for EM noise suppression in frequency bands relevant to 5G technology and could prompt more studies on the superparamagnetic relaxation behavior of nanocrystalline ferrite films and particles.

See the [supplementary material](#) for lattice parameter and crystalline size calculation from XRD data, XPS analysis, additional DC magnetic measurements, and permeability measurements.

The authors acknowledge MNCF (Micro Nano Characterization Facility), CeNSE, IISc, for the Instrumentation Facility, and ISRO, Department of Space, Government of India for the partial financial support to the project. It is also supported partially by the DST-JSPS joint bilateral research project.

AUTHOR DECLARATIONS

Conflict of Interest

The authors have no conflict of interest.

Author Contributions

Sarath Arackal: Conceptualization (equal); Data curation (equal); Formal analysis (equal); Investigation (equal); Methodology (equal); Writing – original draft (equal); Writing – review and editing (equal). **Kouhei Nozawa:** Data curation (equal); Formal analysis (equal); Investigation (equal); Methodology (equal). **Ralandinliu Kahmei:** Data curation (equal); Formal analysis (equal); Investigation (equal); Methodology (equal). **Ton That Loi:** Data curation (equal);

Formal analysis (equal); Methodology (equal); Software (equal). **Shin Yabukami:** Funding acquisition (equal); Resources (equal); Supervision (equal). **S A Shivashankar:** Funding acquisition (equal); Resources (equal); Supervision (equal); Writing – original draft (equal); Writing – review and editing (equal). **Masahiro Yamaguchi:** Funding acquisition (equal); Resources (equal); Supervision (equal). **Navakanta Bhat:** Funding acquisition (equal); Resources (equal); Supervision (equal). **Ranajit Sai:** Conceptualization (equal); Formal analysis (equal); Methodology (equal); Resources (equal); Supervision (equal); Writing – original draft (equal); Writing – review and editing (equal).

DATA AVAILABILITY

The data that support the findings of this study are available within the article and its [supplementary material](#).

REFERENCES

- ¹J. Smit and H. P. J. Wijn, *Ferrites, Physical Properties of Ferrimagnetic Oxides in Relation to their Technical Applications* (Wiley, New York, 1959), OCLC/WorldCat: 1337585.
- ²Y. Zhuang, M. Vroubel, B. Rejaei, J. N. Burghartz, and K. Attenborough, *J. Appl. Phys.* **99**, 08C705 (2006).
- ³F. Ma, Y. Qin, and Y.-Z. Li, *Appl. Phys. Lett.* **96**, 202507 (2010).
- ⁴A. El-Ghazaly, R. M. White, and S. X. Wang, *J. Appl. Phys.* **117**, 17E502 (2015).
- ⁵L. Yuan, Z. Yue, S. Meng, and L. Li, *Phys. Status Solidi A* **211**, 1828 (2014).
- ⁶R. Kumar, B. Samantaray, and Z. Hossain, *J. Phys.: Cond. Matter* **31**, 435802 (2019).
- ⁷B. Z. Rameev, A. Gupta, F. Yildiz, L. R. Tagirov, and B. Aktaş, *J. Magn. Magn. Mater.* **300**, e526 (2006).
- ⁸R. Ade, Y. S. Chen, C.-H. Huang, and J. G. Lin, *J. Appl. Phys.* **127**, 113904 (2020).
- ⁹S. Li, Z. Huang, J.-G. Duh, and M. Yamaguchi, *Appl. Phys. Lett.* **92**, 092501 (2008).
- ¹⁰S. Yuan, B. Kang, L. Yu, S. Cao, and X. Zhao, *J. Appl. Phys.* **105**, 063902 (2009).
- ¹¹N. N. Phuoc, L. T. Hung, and C. K. Ong, *J. Alloys Compd.* **506**, 504 (2010).
- ¹²S. Li, G.-X. Miao, D. Cao, Q. Li, J. Xu, Z. Wen, Y. Dai, S. Yan, and Y. Lü, *ACS Appl. Mater. Interfaces* **10**, 8853 (2018).
- ¹³N.-N. Song, H.-T. Yang, H.-L. Liu, X. Ren, H.-F. Ding, X.-Q. Zhang, and Z.-H. Cheng, *Sci. Rep.* **3**, 3161 (2013).
- ¹⁴D. Hasegawa, H. Yang, T. Ogawa, and M. Takahashi, *J. Magn. Magn. Mater.* **321**, 746 (2009).
- ¹⁵X. Zhang, Y. Liu, and G. Qin, *Appl. Phys. Lett.* **106**, 033105 (2015).
- ¹⁶X. F. Zhang, J. J. Guo, and G. W. Qin, *Appl. Phys. Lett.* **104**, 252404 (2014).
- ¹⁷H. Yuan, Y. Xu, H. Jia, and S. Zhou, *RSC Adv.* **6**, 67218 (2016).
- ¹⁸N. Song, S. Gu, J. Zhou, W. Xia, P. Zhang, Q. Gul, W. Wang, H. Yang, and Z. Cheng, *Appl. Phys. Lett.* **111**, 133108 (2017).
- ¹⁹O. Obi, M. Liu, J. Lou, S. Stoute, X. Xing, N. X. Sun, J. Warzywoda, A. Sacco, D. E. Oates, and G. F. Dionne, *J. Appl. Phys.* **109**, 07E527 (2011).
- ²⁰Y. Yasukawa, K. Nozawa, T. Tiittanen, M. Karppinen, J. Lindén, S. E. Shirsath, and S. Yabukami, *Sci. Rep.* **11**, 614 (2021).
- ²¹R. R. Kahmei, R. Sai, S. Arackal, S. A. Shivashankar, and N. Bhat, *IEEE Magn. Lett.* **10**, 1 (2019).
- ²²R. Sai, S. Arackal, R. D. R. Kahmei, N. Bhat, M. Yamaguchi, and S. A. Shivashankar, *AIP Adv.* **10**, 015101 (2020).
- ²³L. Wu, A. Mendoza-Garcia, Q. Li, and S. Sun, *Chem. Rev.* **116**, 10473 (2016).
- ²⁴Y.-J. Zhu and F. Chen, *Chem. Rev.* **114**, 6462 (2014).
- ²⁵H. J. Kitchen, S. R. Vallance, J. L. Kennedy, N. Tapia-Ruiz, L. Carassiti, A. Harrison, A. G. Whittaker, T. D. Drysdale, S. W. Kingman, and D. H. Gregory, *Chem. Rev.* **114**, 1170 (2014).
- ²⁶R. Sai, K. J. Vinoy, N. Bhat, and S. A. Shivashankar, *IEEE Trans. Magn.* **49**, 4323 (2013).
- ²⁷S. Brahma and S. A. Shivashankar, *Thin Solid Films* **518**, 5905 (2010).
- ²⁸L. Wang and F. S. Li, *J. Magn. Magn. Mater.* **223**, 233 (2001).
- ²⁹A. Zelenáková, J. Kováč, and V. Zelenák, *J. Appl. Phys.* **108**, 034323 (2010).
- ³⁰K. Rumpf, P. Granitzer, P. M. Morales, P. Poelt, and M. Reissner, *Nanoscale Res. Lett.* **7**, 445 (2012).
- ³¹J. C. Denardin, A. L. Brandl, M. Knobel, P. Panissod, A. B. Pakhomov, H. Liu, and X. X. Zhang, *Phys. Rev. B* **65**, 064422 (2002).
- ³²S. Yabukami, K. Nozawa, L. Tonthat, K. Okita, and R. Sai, *IEEE Trans. Magn.* **57**, 1 (2021).
- ³³S. Yabukami, K. Kusunoki, H. Uetake, H. Yamada, T. Ozawa, R. Utsumi, T. Morizumi, and Y. Shimada, *J. Magn. Soc. Jpn.* **41**, 25–28 (2017).
- ³⁴H. Su, H. Zhang, X. Tang, and Y. Jing, *J. Appl. Phys.* **103**, 093903 (2008).
- ³⁵J. Hwang, M. Choi, H.-S. Shin, B.-K. Ju, and M. Chun, *Appl. Sci.* **10**, 6279 (2020).
- ³⁶T. Tsutaoka, *J. Appl. Phys.* **93**, 2789 (2003).
- ³⁷T. Tsutaoka, M. Ueshima, T. Tokunaga, T. Nakamura, and K. Hatakeyama, *J. Appl. Phys.* **78**, 3983 (1995).
- ³⁸T. Tsutaoka, T. Nakamura, and K. Hatakeyama, *J. Appl. Phys.* **82**, 3068 (1997).
- ³⁹T. Nakamura, *J. Appl. Phys.* **88**, 348 (2000).
- ⁴⁰A. Saini, A. Thakur, and P. Thakur, *J. Mater. Sci.* **27**, 2816 (2016).
- ⁴¹A. Omelyanchik, M. Salvador, F. D’Orazio, V. Marni, C. Cannas, D. Fiorani, A. Musinu, M. Rivas, V. Rodionova, G. Varvaro, and D. Peddis, *Nanomaterials* **10**, 1288 (2020).
- ⁴²Y. Komorida, M. Mito, H. Deguchi, S. Takagi, A. Millán, N. J. O. Silva, and F. Palacio, *Appl. Phys. Lett.* **94**, 202503 (2009).
- ⁴³D. S. Schmool, R. Rocha, J. B. Sousa, J. A. M. Santos, and G. Kakazei, *J. Magn. Magn. Mater.* **300**, e331 (2006).
- ⁴⁴S. Thota, S. C. Kashyap, S. K. Sharma, and V. R. Reddy, *J. Phys. Chem. Solids* **91**, 136 (2016).
- ⁴⁵Z. Beji, T. Ben Chaabane, L. S. Smiri, S. Ammar, F. Fiévet, N. Jouini, and J. M. Grenèche, *Phys. Status Solidi A* **203**, 504 (2006).
- ⁴⁶D. V. Kurmude, R. S. Barkule, A. V. Raut, D. R. Shengule, and K. M. Jadhav, *J. Supercond. Novel Magn.* **27**, 547 (2014).
- ⁴⁷J. J. Thomas, A. B. Shinde, P. S. R. Krishna, and N. Kalarikkal, *J. Alloys Compd.* **546**, 77 (2013).
- ⁴⁸S. A. Morrison, C. L. Cahill, E. E. Carpenter, S. Calvin, R. Swaminathan, M. E. McHenry, and V. G. Harris, *J. Appl. Phys.* **95**, 6392 (2004).
- ⁴⁹S. M. Rezende, A. Azevedo, and R. L. Rodríguez-Suárez, *J. Appl. Phys.* **126**, 151101 (2019).
- ⁵⁰S. Emori and P. Li, *J. Appl. Phys.* **129**, 020901 (2021).